



# The activation of reactants and intermediates promotes the selective photocatalytic NO conversion on electron-localized Sr-intercalated g-C<sub>3</sub>N<sub>4</sub>

Xing'an Dong<sup>a</sup>, Jieyuan Li<sup>b</sup>, Qian Xing<sup>a</sup>, Ying Zhou<sup>c</sup>, Hongwei Huang<sup>d</sup>, Fan Dong<sup>a,c,\*</sup>

<sup>a</sup> Chongqing Key Laboratory of Catalysis and New Environmental Materials, College of Environment and Resources, Chongqing Technology and Business University, Chongqing 400067, China

<sup>b</sup> College of Architecture and Environment, Institute of New Energy and Low Carbon Technology, Sichuan University, Chengdu, Sichuan 610065, China

<sup>c</sup> The Center of New Energy Materials and Technology, School of Materials Science and Engineering, Southwest Petroleum University, Chengdu 610500, China

<sup>d</sup> Beijing Key Laboratory of Materials Utilization of Nonmetallic Minerals and Solid Wastes, National Laboratory of Mineral Materials, School of Materials Science and Technology, China University of Geosciences, Beijing 100083, China

## ARTICLE INFO

### Keywords:

Reactants activation  
Electron localization  
Selective photocatalysis  
NO oxidation  
In situ  
DRIFTS

## ABSTRACT

Photocatalysis technology has been widely adapted to address air pollution. However, the photocatalysis efficiency and selectivity should be optimized to achieve efficient and safe air purification. Take the g-C<sub>3</sub>N<sub>4</sub> (CN) as a case study, in order to promote the photocatalytic performance and the selectivity of g-C<sub>3</sub>N<sub>4</sub> in oxidizing NO into target products of NO<sub>2</sub><sup>−</sup> and NO<sub>3</sub><sup>−</sup>, the electron localization has been built in Sr-intercalated g-C<sub>3</sub>N<sub>4</sub> (CN-Sr) to promote the activation of reactants and intermediates, as well as the charge separation and transfer. The intercalated Sr atom causes the uneven electron distribution on the plane of CN. The O<sub>2</sub> could capture the localized excess electrons and be activated producing ·O<sub>2</sub><sup>−</sup> radicals. The NO and the reaction intermediates could deplete the electrons more easily and be activated on the surface of CN-Sr. The activated species possess longer bond length and have higher reactivity during photocatalysis, making them easier to be destroyed by active radicals and transforming to target products of NO<sub>2</sub><sup>−</sup> and NO<sub>3</sub><sup>−</sup> rather than other toxic byproducts. With the pivotal effect of localized electrons in CN-Sr, the photocatalytic activity and selectivity can be simultaneously promoted. With the in situ DRIFTS investigation and theoretical calculation, the present work specified the transportation and transformation of photogenerated carriers and revealed the mechanism of photocatalytic NO oxidation. This work could provide a new approach to enhance the photocatalytic activity and selectivity for efficient and safe air pollution control.

## 1. Introduction

Nitrogen oxide (NO<sub>x</sub>) emitted from coal-fired combustion is one of the typical air pollutants responsible for urban smog and acid rain. Therefore, the removal of NO<sub>x</sub> in air has become a major goal in the past few years [1]. Compared to traditional technologies (adsorption, absorption, SCR), photocatalysis as a green technology has displayed great potential in solving the NO<sub>x</sub> pollution problems [2–7].

Photocatalysis has been considered as a nonselective process for pollutants degradation, and the investigation on selective photocatalysis has been largely neglected [8–11]. Recently, the field of selective photocatalysis is developing rapidly in degradation of typical pollutants [12–16], which is an effective pathway to remove pollutants at low concentration [17–20]. However, in photocatalytic NO oxidation, the selectivity has been less investigated because of the difficulty

in quantifying the amount of target products NO<sub>2</sub><sup>−</sup> and NO<sub>3</sub><sup>−</sup>. For instance, LaFeO<sub>3</sub>-SrTiO<sub>3</sub> composite photocatalyst was prepared to remove NO and the yield of toxic byproduct NO<sub>2</sub> was noticed, but the selectivity has not been concerned [21]. Moreover, the selective NO oxidation on BiOI surface has also been researched, and the production of NO<sub>3</sub><sup>−</sup> had been compared by FT-IR method [22]. However, the reaction mechanism of photocatalytic NO oxidation has not been fully revealed. In this work, the in situ DRIFTS are adopted here to quantify the yield of absorbed target products and to investigate the selectivity and reaction mechanism of photocatalytic NO oxidation.

In order to selectively transform NO to form target products via photocatalytic oxidation, improving the oxidation capacity of photo-induced radicals is the most direct way. Tuning the amount of reactive oxygen species (ROS) and electronic structure are effective methods to promote the activation of reactants and further enhance the

\* Corresponding author: Chongqing Key Laboratory of Catalysis and New Environmental Materials, College of Environment and Resources, Chongqing Technology and Business University, Chongqing 400067, China.

E-mail address: [dfctbu@126.com](mailto:dfctbu@126.com) (F. Dong).

<https://doi.org/10.1016/j.apcatb.2018.03.054>

Received 28 January 2018; Received in revised form 1 March 2018; Accepted 18 March 2018

Available online 19 March 2018

0926-3373/ © 2018 Elsevier B.V. All rights reserved.

photocatalytic selectivity [23–25]. Here, the g-C<sub>3</sub>N<sub>4</sub> (CN) was investigated as a model photocatalyst because of its visible-light response, excellent stability and adjustable electronic structure [26–33]. The alkali metal can be intercalated in the planes of CN, which could bridge the adjacent layers of CN to build an electrons delivery channel and induce the formation of localized electrons [34,35]. The random distributed electrons on a plane could be localized to intercalated element atom and assemble localized excess electrons in high electron density region. Outside of electron-localized region, low electron density area is formed. As a result, the O<sub>2</sub> could capture excess electrons from localized region and the NO could donate electrons to low electron density area. In this way, both the O<sub>2</sub> and NO can be activated, contributing to the enhanced photocatalytic selectivity.

On the basis of the above consideration, we theoretically designed the Sr-intercalated g-C<sub>3</sub>N<sub>4</sub> (CN-Sr, for simulated calculation structure, similarly hereinafter) in an attempt to enhance the electron localization. With the localized excess electrons, the activation of reactants and intermediate products can be promoted and the selectivity could be further elevated. Combining with the methods of free radical trapping, in situ DRIFTS and DFT calculation, the evolution process of intermediate products during photocatalytic NO oxidation were clarified. Subsequently, the CN-Sr was prepared and the photocatalytic NO oxidation process was dynamically monitored. Because of intercalated Sr atoms between CN layers, the vertical charge channel was built and charge separation efficiency was accelerated. More importantly, the electron localization could lead to uneven electron distribution in the CN plane. In combination with in situ DRIFTS and DFT simulation, the O<sub>2</sub> molecules are found to capture electrons at electron-localization area to form  $\cdot\text{O}_2^-$ . The NO and intermediate products could deplete electrons to low electron density region easily. As a result, all these reactants and intermediates can be activated and react with the radicals to form target products rather than toxic byproducts. The present work could provide new approaches to enhanced photocatalytic activity and selectivity achieving efficient and safe air purification.

## 2. Experimental

### 2.1. Materials and fabrication

All chemicals used in this work were analytical grade and without further treatment. Sr intercalated g-C<sub>3</sub>N<sub>4</sub> were synthesized by a facile co-pyrolysis method, using thiourea and Sr(NO<sub>3</sub>)<sub>2</sub> were used as starting materials. 10 g thiourea and a given amount Sr(NO<sub>3</sub>)<sub>2</sub> (3, 5, 10 wt %, relative to the experimentally obtained g-C<sub>3</sub>N<sub>4</sub>) were added in an alumina crucible with 30 mL distilled water. The obtained blended reagents were subsequently dried at 80 °C overnight to recrystallize precursors. And then the crucible with a cover was calcined at 550 °C in air for 2 h with a heating rate of 15 °C min<sup>-1</sup>. After naturally cooling down to room temperature, the pristine g-C<sub>3</sub>N<sub>4</sub> and Sr intercalated g-C<sub>3</sub>N<sub>4</sub> with different weight ratio (3, 5, 10 wt %) are labeled as CN, CN-3Sr, CN-5Sr and CN-10Sr, respectively.

### 2.2. Characterization

The crystal phases of the samples were analyzed by X-ray diffraction (XRD) with Cu K $\alpha$  radiation (model D/max RA, Rigaku Co., Japan). X-ray photoelectron spectroscopy (XPS) with Al K $\alpha$  X-rays (Thermo ESCALAB 250, U. S. A.) was used to investigate the surface properties. The morphology and structure of the samples were examined by scanning electron microscopy (SEM, model JSM-6490, JEOL, Japan) and transmission electron microscopy (TEM, JEM-2010, Japan). The UV–vis diffuse-reflectance spectrometry (UV–vis DRS) spectra were obtained for the dry-pressed disk samples using a scanning UV–vis spectrophotometer (UV2550, Shimadzu, Japan) equipped with an integrating sphere assembly, using 100% BaSO<sub>4</sub> as the reflectance sample. Nitrogen adsorption-desorption isotherms were obtained on a

nitrogen adsorption apparatus (ASAP 2020, U.S.A.) with all samples degassed at 300 °C for 4 h before measurements. Photoluminescence (PL) studies (F-7000, HITACHI, Japan) were conducted to investigate the optical properties of the samples. Steady and time-resolved fluorescence emission spectra were recorded at room temperature with a fluorescence spectrophotometer (Edinburgh Instruments, FLSP-920). Electron spin resonance (ESR) of radicals spin-trapped by 5, 5-dimethyl-1-pyrroline N-oxide (DMPO) were recorded on a JES FA200 spectrometer. Samples for ESR measurement were prepared by mixing the samples in a 40 mM DMPO solution tank (aqueous dispersion for DMPO- $\cdot\text{OH}$  and methanol dispersion for DMPO- $\cdot\text{O}_2^-$ ) and irradiated with visible light. Electron paramagnetic resonance (EPR) measurements were carried out on a Bruker ESP 500 spectrometer.

### 2.3. Evaluation of visible-light photocatalytic activity

The photocatalytic activity was investigated by removal ratio of NO at ppb levels in a continuous-flow reactor at the ambient temperature. The volume of the rectangular reactor, which is made of polymeric glass and covered with Saint-Glass, was 4.5 L (30 cm  $\times$  15 cm  $\times$  10 cm). A 150 W commercial tungsten halogen lamp was vertically placed outside the reactor. A UV cutoff filter (420 nm) was utilized to remove the UV light in the light beam. For each test, 0.20 g of the prepared sample was dispersed in distilled water (50 mL) in a beaker via ultrasonic treatment for dispersion and then coated onto two glass dishes (12.0 cm in diameter). The coated dish was dried at 60 °C to remove water and then cooled to room temperature before the test.

The NO gas was obtained from a compressed gas cylinder at a concentration of NO was diluted to about 600 ppb by the air stream. The desired relative humidity level of the NO flow was controlled at 50% by passing the zero air streams through a humidification chamber. The gas streams were premixed completely by a gas blender, and the flow rates of the air stream and NO were controlled at 2.4 L min<sup>-1</sup> and 24 mL min<sup>-1</sup>, respectively, by a mass flow controller. After the adsorption-desorption equilibrium was achieved, the lamp was turned on. The concentration of NO was continuously measured by a NO<sub>x</sub> analyzer (Thermo Environmental Instruments Inc., model 42c-TL). The removal ratio ( $\eta$ ) of NO was calculated as  $\eta$  (%) =  $(1 - C/C_0) \times 100\%$ , where  $C$  and  $C_0$  are concentrations of NO in the outlet steam and the feeding stream, respectively.

### 2.4. In situ DRIFTS study on photocatalytic NO oxidation process

In situ DRIFTS measurements were conducted using the Tensor II FT-IR spectrometer (Bruker) equipped with an in situ diffuse reflectance cell (Harrick) and shown in Scheme S1. Photocatalysts were put into the reaction cell. First, the He gas (100 mL/min) was used to remove the residual hydrocarbons, H<sub>2</sub>O and CO<sub>2</sub> under 300 °C. The real-time FT-IR spectrum after ventilation was utilized as background. Then, the reaction mixtures (50 mL/min NO, 50 mL/min O<sub>2</sub>) were introduced into the cell. The NO adsorption on the catalysts was carried out for 20 min. Next, photocatalysts were illuminated by visible light source (MUA-210) for 1 h. The real-time FT-IR spectra were detected every eight minutes. Meanwhile the gas fluxes keep the same (50 mL/min NO, 50 mL/min O<sub>2</sub>). Finally, FT-IR spectra were recorded every two minutes with the same gas fluxes after turning off the light. The IR scanning range was 4000–600 cm<sup>-1</sup>. The intervals 2250–2000 cm<sup>-1</sup> and 1120–840 cm<sup>-1</sup> were analyzed to present the photocatalytic oxidation process on the catalysts.

### 2.5. DFT calculations

Spin-polarized DFT-D2 calculations[36] were conducted using the “Vienna *ab initio* simulation package” (VASP5.4) [37,38], applying a generalized gradient correlation functional [39]. A plane-wave basis set with cut-off energy 450 eV within the framework of the projector-

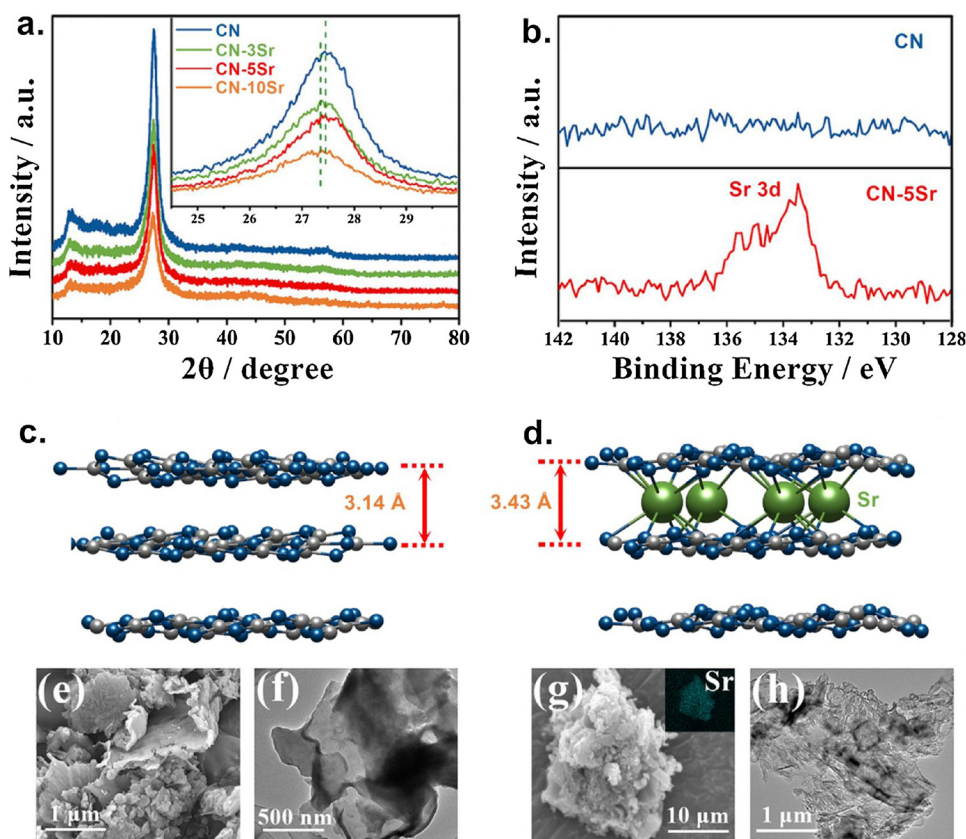


**Fig. 1.** Crystal structure and morphology of  $g\text{-C}_3\text{N}_4$  and Sr intercalated  $g\text{-C}_3\text{N}_4$ . XRD pattern of four as-prepared samples, the inset is the enlarged profile of the {002} diffraction region (a); XPS spectra of Sr 3d (b); optimized local structures of bulk-CN sample; (c); optimized local structures of Sr intercalated samples, blue, grey and green spheres depict N, C and Sr atoms, respectively (d); SEM image of CN (e); TEM image of CN (f); SEM image of CN-5Sr, the inset is FESEM-EDX elemental mapping of CN-5Sr (g); TEM image of CN-5Sr (h) (For interpretation of the references to colour in this figure legend, the reader is referred to the web version of this article).

augmented wave method was employed [40,41]. The Gaussian smearing width was set to 0.2 eV. The Brillouin zone was sampled with a  $3 \times 3 \times 1$  Monkhorst Pack grid. All atoms were converged to 0.01 eV  $\text{\AA}^{-1}$ . Hybrid functional based on the Heyd-Scuseria-Ernzerhof (HSE06) method [42,43] were applied to estimate the exact band structures.

The adsorption energy ( $E_{\text{ads}}$ ) is defined as

$$E_{\text{ads}} = E_{\text{tot}} - (E_{\text{CN}} + E_{\text{mol}}) \quad (1)$$

Where  $E_{\text{tot}}$ ,  $E_{\text{CN}}$  and  $E_{\text{mol}}$  depict the total energy of the adsorption complex, the pure CN and the isolated molecule, respectively.

### 3. Results and discussion

#### 3.1. Materials and structures

In order to establish a vertical charge channel between the CN layers to better promote the activation of reactants and intermediates, the Sr intercalated CN samples were synthesized on the basis of our previous study [34,44,45]. XRD patterns (Fig. 1a) represent the existence of graphitic-like layers with two characteristic diffraction peaks at  $13.1^\circ$  and  $27.4^\circ$ , corresponding to {100} and {002} planes, respectively. The slight leftshift of {002} peaks of Sr intercalated CN compared with the pristine CN is observed (Fig. 1a inset), which can be attributed to the incorporation of Sr atom between the CN layers.

The nitrogen adsorption-desorption isotherms for Sr doped  $g\text{-C}_3\text{N}_4$  are type IV with H3 hysteresis loops, suggesting the presence of slit-shaped pores originating from the aggregation of platelike particles (Fig. S1). Also, the pore size distribution curves in Fig. S1 (inset) show that the as-prepared three Sr-doped samples contain small mesopores at 3.7 nm and some macropores. The specific surface areas for CN-3Sr, CN-5Sr, CN-10Sr are 18.5, 13.3 and 9.1  $\text{m}^2 \text{g}^{-1}$ , respectively, slightly lower than that of pristine  $g\text{-C}_3\text{N}_4$  (23.0  $\text{m}^2 \text{g}^{-1}$ ).

Moreover, it is noted that Sr element is well identified with binding energy located at its corresponding peak in the XPS spectra (Fig. 1b).

The Sr element with binding energy is located at 133.5 eV corresponding to the Sr 3d peak in CN-5Sr, suggesting the presence of the Sr species. When Sr is introduced, the outermost electrons are transferred to  $g\text{-C}_3\text{N}_4$ , inducing a static coulomb interaction between Sr and N (C) and the form of Sr–N and Sr–C bonds. (Fig. S2). In addition, XPS spectra of C and N elements between CN and CN-5Sr samples (Fig. S3) reveal that the crystal structure of  $g\text{-C}_3\text{N}_4$  is not damaged after the doping of Sr atoms.

The electronic structure of Sr intercalated  $g\text{-C}_3\text{N}_4$  is further investigated by the DFT calculation. The results imply that Sr atoms are stably intercalated between adjacent CN layers (Fig. 1c and d) by the proof of the increased heat release compared to those in CN planes. Notably, the layer distance of CN are enlarged in the order of CN (3.14  $\text{\AA}$ ) < N–Sr (3.43  $\text{\AA}$ ) which matches well with the XRD patterns. The typical SEM and TEM images (Fig. 1e–h) illustrate that CN-5Sr is composed of curved layers, which are similar to CN, suggesting that the introduction of Sr does not influence the morphology. The Sr signal can be detected in the element mapping of CN-5Sr (Fig. 1g inset), verifying the homogeneous dispersion of Sr elements across the selected area.

#### 3.2. Optical properties and energy band structure

In order to investigate the effects of interlayered Sr-doping on the optical properties and the energy band structure of  $g\text{-C}_3\text{N}_4$ , the light adsorption property of as-prepared samples is firstly investigated by UV–vis diffuse reflectance spectra (Fig. 2a). In contrast to the pristine CN, the red-shifted adsorption edge can be observed in Sr intercalated CN, which enables the extended light adsorption due to Sr-doping. The elevated light harvest could also be certified via the calculated adsorption spectra (Fig. 2b), which is in good accordance with the experimental results. The broadened adsorption ability endows the photocatalyst with more photons obtainment, generating more photo-excited carriers. The density of state (DOS) is subsequently calculated (Fig. 2c) to estimate the band energy. After Sr-doping, the band gap has

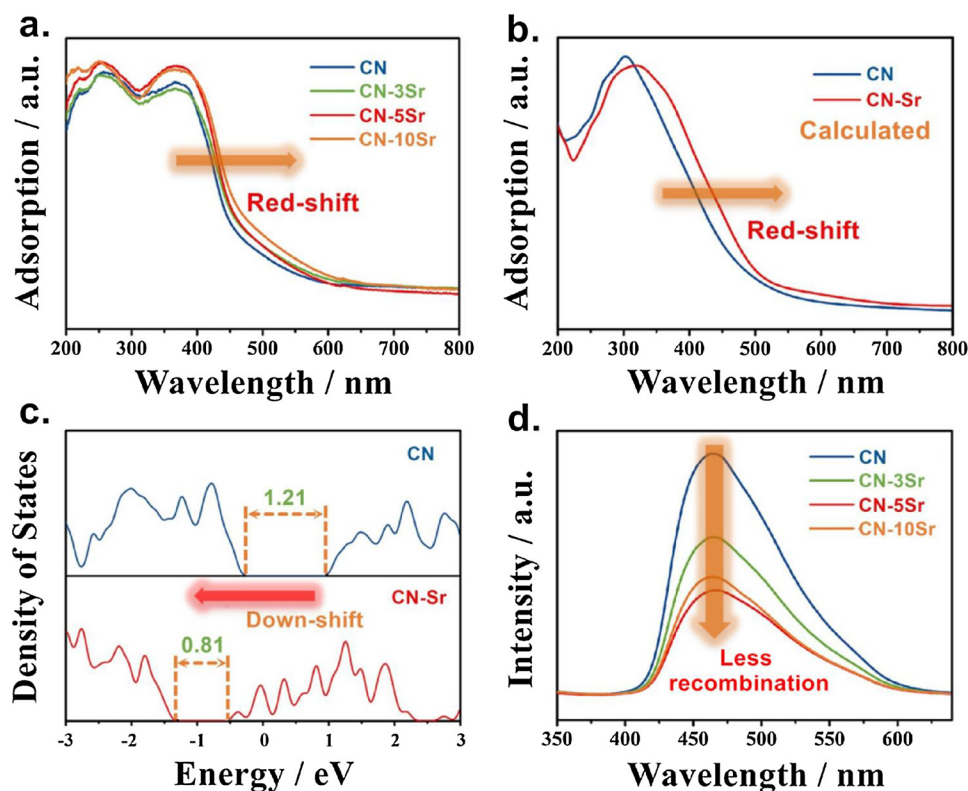


Fig. 2. The UV-vis spectra (a); the calculated adsorption spectra (b) and density of states (DOS), the Fermi level is set to 0 eV (c); PL spectra of four as-prepared samples (d).

become narrowed obviously, consistent the red shift of adsorption edge. Notably, the calculated band gap energy for g-C<sub>3</sub>N<sub>4</sub> is lower than experimental one, which has been also reported in literature. It is a consequence of the fact that DFT calculation usually underestimates the energy gaps for its own limitation because of the discontinuity in the exchange-correlation potential [46]. The valence band (VB) and conduction band (CB) edges of CN-Sr down-shift relative to those of the pristine CN, which indicates that the band structure of CN can be tailored by the Sr mediator.

Satisfactorily, the narrowed band gap doesn't bring higher recombination efficiency of light-generated electrons and holes, which is certified by the PL spectra (Fig. 2d). The optimized band structure and the enhanced charge separation can be achieved simultaneously on the Sr intercalated CN.

### 3.3. Electron localization and charge transportation

The charge separation and transportation properties are examined to support the high electrons-hole separation efficiency because of the electron localization. The low temperature solid state electrons paramagnetic resonance (EPR, Fig. 3a) implies that only one single Lorentzian line centered at g value of 2.0 is noted for both samples, which indicates the existence of intrinsic defects [47]. Moreover, the extension of the graphitic  $\pi$ -conjugation system is enhanced in CN-5Sr. Under visible light irradiation, the EPR signals are increased for both samples, indicating that the electron mobility is promoted in the  $\pi$ -conjugation system. The establishment of interlayer electronic channel leads to broadened band distribution and accelerated electrons mobility, which promotes the charge exchange between the photocatalyst and reactants. Detailed electron transfer direction is illustrated from the electrostatic potential energy (Fig. 3b). The potential energy of the first layer and subsurface CN layer in CN-Sr are increased in comparison with those of the pristine CN. The potential difference between layers essentially provides the intrinsic driving force for electrons migration in a one-way transfer channel in vertical direction, resulting in the spatial charge

separation.

Furthermore, the charge difference distribution between Sr atoms and CN layers is shown in Fig. 3c. It can be found that the random distributed electrons on surface layer are localized to Sr atom and form a local region with high electron density. Then, these localized excess electrons transfer to the sublayer via the Sr-mediated electronic channel. For the purpose of illustrating the effect of electron localization more intuitively, the carried charges ( $\Delta q$ ) of atoms around Sr atom are calculated with Bader methods (Fig. 4) [48]. Apparently, the C and N atoms around Sr atom of CN-Sr model possess more electrons in contrast to pristine CN model, which further confirms the intercalated Sr atom enable the localization of the electrons around.

In addition, the interlayered electronic channel could strengthen the electron transfer directionally mediated by Sr in the interlayer (Fig. S2), which results in the generation of oriented internal electric field (OIEF) and effectively facilitation of the interlayered charge flow, thus enormously impeding the spatial recombination of electron-hole pairs. The time-resolved fluorescence decay spectrum is further employed to investigate the charge motion dynamics with curves fitted via the Biexponential decay function (Fig. 3d). Obviously, in contrast to the pristine CN, the lifetime of charge carriers in CN-5Sr is prolonged from 6.05 ns to 7.62 ns, suggesting that the formation of electron localization and interlayered electrons transfer channel could effectively boost the charge transfer and provide the kind of easily trapped localized electrons. The localized electrons could increase their probability to participate in the activation of reactants and intermediates.

### 3.4. Photocatalysis activity, selectivity and mechanism

The photocatalytic oxidation performances of pristine CN and Sr intercalated CN samples have been surveyed toward the NO removal under visible-light irradiation (Fig. 5a). For all four samples, the NO removal ratios are increased in the order of CN (36.3%) < N-10Sr (44.7%) < N-3Sr (50.9%) < N-5Sr (53.1%) after 30 minutes irradiation. This result implies that the Sr-doping could highly increase the



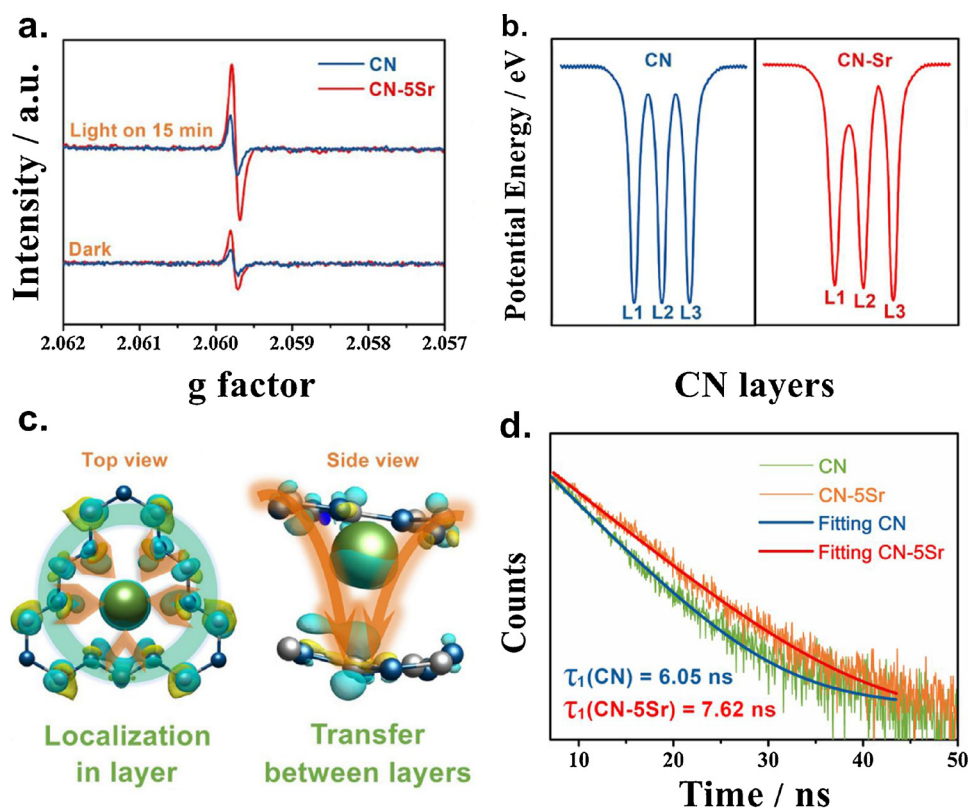


Fig. 3. Low temperature EPR spectra (a); electrostatic potential (b); charge difference distribution between Sr atoms and CN layers: charge accumulation is in blue and depletion in yellow (c); the ns-level time-resolved fluorescence spectra surveyed at room temperature (d) (For interpretation of the references to colour in this figure legend, the reader is referred to the web version of this article).

photocatalysis efficiency of g-C<sub>3</sub>N<sub>4</sub> ascribing to the enhanced charge separation and transfer (Figs. 2 and 3).

For photocatalytic NO oxidation, the radicals play a vital role in NO removal process. Hence, the mechanism of O<sub>2</sub> activation is simulated by DFT calculations. In comparison with the pristine CN (Fig. 5a), the O–O bond length is apparently enlarged from 1.25 Å of pristine CN to 1.39 Å of Sr intercalated CN, which results in the weakened Coulomb interaction of gas molecules on the catalyst surface, thus leading to increased adsorption energy from −0.12 eV to −1.95 eV. It is obvious that the O<sub>2</sub> molecule could capture more electrons from Sr intercalated CN than pristine CN according to the charge difference distribution calculation. The enlarged O–O bond and increasing adsorption energy both imply that the O<sub>2</sub> molecule receives more localized electrons and readily activated to form  $\cdot\text{O}_2^-$  radicals. It is further proven by electronic localization function (ELF) that the covalent interaction in O–C is intensified (Fig. S2), so the O<sub>2</sub> molecules can be easily activated on the surface of CN-Sr (Fig. 5b). Most importantly, it is notable that the

carried charge  $\Delta q$  is indubitably increased in the order of CN (0.08 e) < CN-Sr (0.81 e), which implies that localized electrons could easily be captured by O<sub>2</sub> molecule and O<sub>2</sub> is readily activated.

The DMPO spin-trapping ESR is then elaborated to fully determine the reactive species that account for the activity enhancement. As shown in Fig. 5c, the stronger signals of light-induced DMPO- $\cdot\text{O}_2^-$  can be detected for CN-5Sr in comparison with CN. The increased  $\cdot\text{O}_2^-$  radicals are crucially dependent on the localized electrons, which enable the O<sub>2</sub> molecules obtaining more electrons for enhanced activation. In addition, the increased DMPO- $\cdot\text{OH}$  is also observed in CN-5Sr (Fig. 5d). The formation of  $\cdot\text{OH}$  originates from the reduction of  $\cdot\text{O}_2^-$  in the path of  $\cdot\text{O}_2^- \rightarrow \text{H}_2\text{O}_2 \rightarrow \cdot\text{OH}$ , which again demonstrates that the electrons excitation and charge transportation in CN-5Sr is effectively promoted.

The In situ DRIFTS, which could dynamically monitor the adsorbed reaction intermediates and products in time sequence, are subsequently carried out to intuitively reveal the conversion pathways and reaction

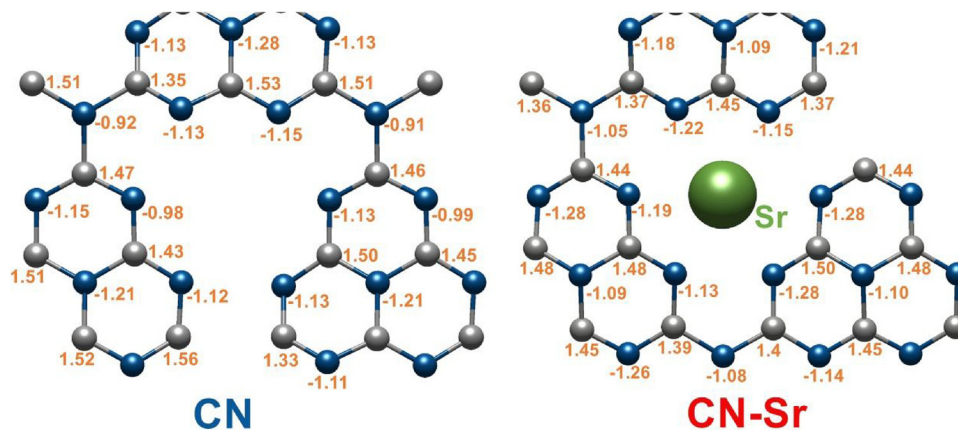


Fig. 4. Carried electrons (c and d) for pristine CN (left) and CN-Sr (right).

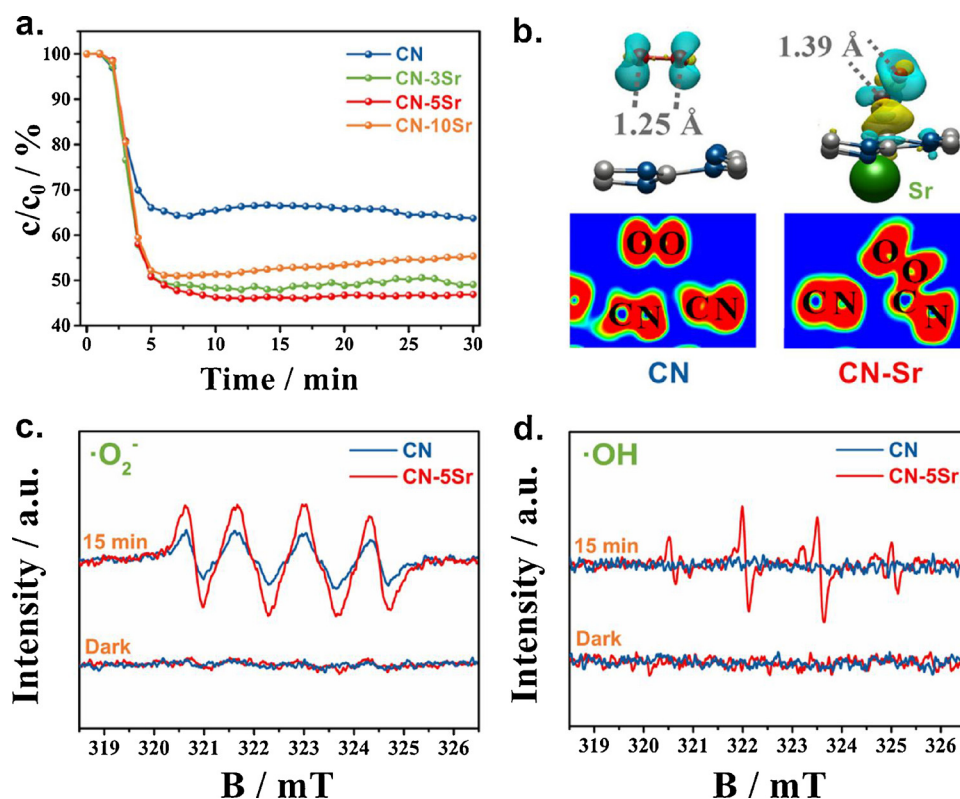


Fig. 5. Photocatalytic activity for NO removal (a); charge difference distribution of optimized  $O_2$  adsorption inbetween  $O_2$  and CN layers: charge accumulation is in blue and depletion in yellow with the isosurfaces set to  $0.005 \text{ eV } \text{\AA}^{-3}$ ; ELF of optimized  $O_2$  adsorption (b); DMPO ESR spectra in dark and under visible-light ( $\lambda \geq 420 \text{ nm}$ ) for 15 minutes in methanol dispersion, respectively for  $\cdot O_2^-$  (c) and aqueous dispersion for  $\cdot OH$  (d) (For interpretation of the references to colour in this figure legend, the reader is referred to the web version of this article).

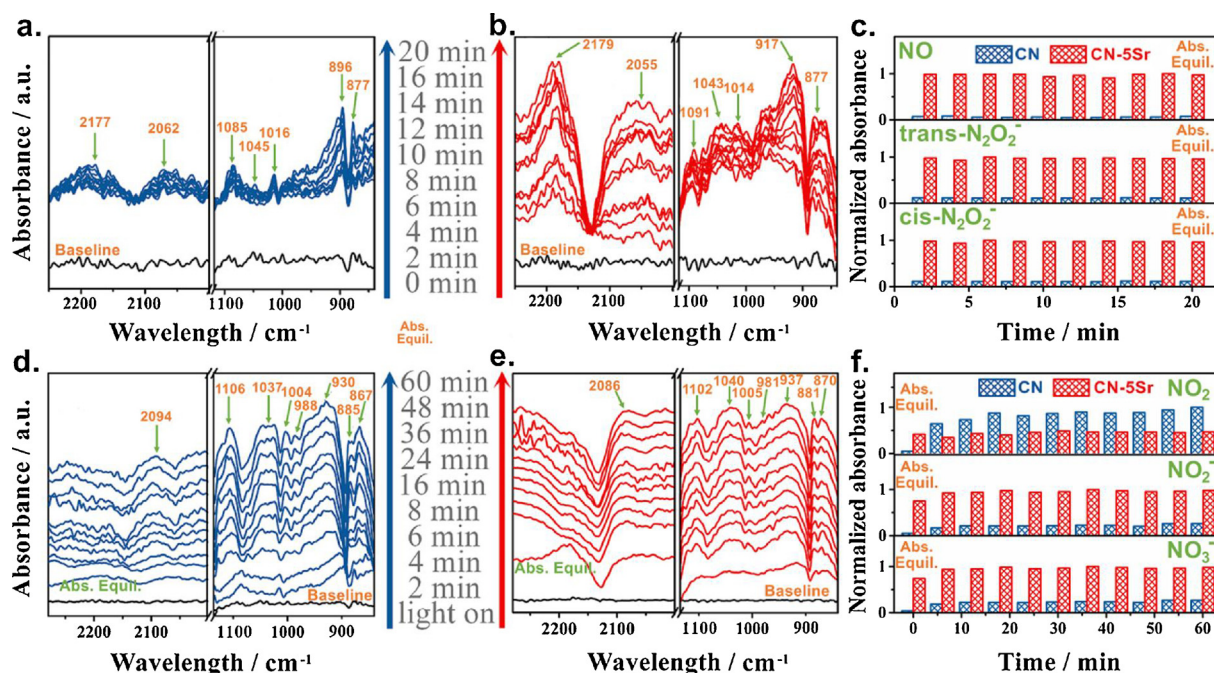


Fig. 6. In situ FT-IR spectra of the adsorption process of NO +  $O_2$  for CN (a) and CN-5Sr (b); the photocatalytic degradation of NO on the surface for CN (d) and under visible light irradiation (e); species evolution of adsorption process (NO,  $\text{trans-N}_2O_2^-$  and  $\text{cis-N}_2O_2^-$ ) (c) and irradiation reaction process ( $NO_2$ ,  $NO_2^-$  and  $NO_3^-$ ) (f).

mechanism for photocatalytic NO oxidation. The NO absorption bands appear immediately after the NO molecules contact with CN at  $25^\circ\text{C}$  in dark condition (Fig. 6a). On the surface of CN, the adsorption band of NO ( $1085 \text{ cm}^{-1}$ ) is observed [49] because of the physical adsorption. Besides,  $\text{cis-N}_2O_2$  at  $1045 \text{ cm}^{-1}$  and  $\text{trans-N}_2O_2$  at  $1016 \text{ cm}^{-1}$  [50] appear as the NO could combine and adsorb on CN. The  $N_2O_2$  can be easily oxidized by  $O_2$  in the atmosphere to produce  $NO_2$  ( $2062 \text{ cm}^{-1}$ ) [51]. Part of these  $NO_2$  are adsorbed on the surface of CN in the form of

$N_2O_4$  ( $2177$  and  $896 \text{ cm}^{-1}$ ) [52] and the other transforms to  $NO_2^-$  ( $877 \text{ cm}^{-1}$ ) [50], which demonstrates that the NO oxidation reaction could proceed slowly without light irradiation. This phenomenon arises from the reactive pyridine N atoms, which preferably donate its lone-pair electrons to  $O_2$  molecules for production of reactive  $\cdot O_2^-$  species. Over time, intensity of aforementioned adsorption bands increases progressively, implying the gradual accumulation of adsorption compounds. In the case of CN-5Sr (Fig. 6b), these adsorption species are

also detected (2179, 2055, 1091, 1043, 1014, 917 and 877  $\text{cm}^{-1}$ ), which implies that the NO adsorption process on CN-5Sr is similar to that of the bare CN with a unified mechanism of NO adsorption on CN. However, intensity of CN-5Sr is much higher than CN, indicates that the Sr doping could improve the adsorption of species.

After achieving the adsorption equilibrium, the time-dependent IR spectra of CN and CN-5Sr are monitored dynamically under visible-light irradiation. As shown in the photocatalytic NO oxidation process on CN (Fig. 6d), the increased adsorption intensity at absorption bands of 2094, 1106, 1037 and 1004  $\text{cm}^{-1}$  are observably detected, which illustrates the accumulation of adsorption species ( $\text{N}_2\text{O}_4$ , NO, cis- $\text{N}_2\text{O}_2$  and trans- $\text{N}_2\text{O}_2$ ). Bands at 885 and 867  $\text{cm}^{-1}$  could be assigned as  $\text{NO}_2^-$ , which is a kind of target product and gradually accumulated on the catalyst surface. In addition, another target product  $\text{NO}_3^-$  is detected at two new peaks at 988 and 930  $\text{cm}^{-1}$  [53]. A similar oxidation process is also obtained on CN-5Sr (Fig. 6e). Notably, further increase of the adsorption intensity at 981  $\text{cm}^{-1}$  ( $\text{NO}_3^-$ ) [51] is markedly observed in comparison with those on the pure CN, which indicates more efficient products generation. The boosted generation of product is in accord with the photocatalytic activity of CN-5Sr and radical production. Note that the nitrate accumulated on the catalyst can be easily removed by water washing [45]. For practical application, the nitrate would be removed by rain water.

Moreover, according to IR spectra in time sequence, the temporal evolution of normalized absorbance of NO, cis- $\text{N}_2\text{O}_2$  and trans- $\text{N}_2\text{O}_2$  during the adsorption process is shown in Fig. 6c. The evolution processes for  $\text{NO}_2$ ,  $\text{NO}_2^-$  and  $\text{NO}_3^-$  during irradiation process on photocatalysts surface are provided in Fig. 6f. For the concerned species, the normalized absorbance is calculated by considering their individual maximum absorbance as one. According to the tendency of species evolution, it can be clearly observed that the adsorption and transformation of NO, intermediates cis- $\text{N}_2\text{O}_2$  and trans- $\text{N}_2\text{O}_2$  are all greatly boosted on CN-5Sr in NO adsorption process, indicating that the Sr doping could promote the ability of NO adsorption and activation. During the irradiation process, two target products  $\text{NO}_2^-$  and  $\text{NO}_3^-$  are greatly increased as well, which implies that the promoted ability of NO activation significantly improved photocatalytic oxidation selectivity for target products. More importantly, the toxic byproduct  $\text{NO}_2$  has been suppressed efficiently on CN-5Sr due to the enhanced oxidation capability. Consequently, the enhanced NO activation accelerates the formation of intermediates and then facilitates the conversion from NO and intermediates to the target products [54,55]. Finally, the selectivity of NO to  $\text{NO}_3^-$  formation has been promoted distinctly.

In order to elaborate the detailed reasons for the enhancement in photocatalysis selectivity reactants (intermediates) activation, DFT calculations were further carried out to analyze the adsorption energies (Table 1) of major detected intermediates and target products on the catalyst surface (Fig. 7 and Figs. S4-S6). For the pristine CN, the adsorption energy of  $\text{NO} \rightarrow \text{cis-}\text{N}_2\text{O}_2 \rightarrow \text{trans-}\text{N}_2\text{O}_2$  process is a increase tendency, which indicates the improved stability of these three species and the reactions of these exothermic processes are energy favorable. However, an energy barrier appears when trans- $\text{N}_2\text{O}_2$  further reacts with the radicals to produce  $\text{NO}_2^-$  and thus this process needs external energy for triggering. And after that, the  $\text{NO}_2^- \rightarrow \text{NO}_3^-$  reaction is easy to proceed due to the relatively large increase in adsorption energy. For Sr intercalated CN, the exotherm quantities of each process are higher

than that of pristine CN. Most striking of all, compared with pristine CN, the energy barrier of trans- $\text{N}_2\text{O}_2$  to  $\text{NO}_2^-$  disappears. The energy profile clearly demonstrate that the whole  $\text{NO} \rightarrow \text{cis-}\text{N}_2\text{O}_2 \rightarrow \text{trans-}\text{N}_2\text{O}_2 \rightarrow \text{NO}_2^- \rightarrow \text{NO}_3^-$  processes are exothermic reactions and are all energy favorable.

The key information of bond lengths of these adsorbed species is also displayed in Fig. 7. It is obvious that all the bond lengths of adsorbed species on CN-Sr are longer than that on pristine CN. Combining with the adsorption energy, the activation of all species on CN-Sr is more efficient than that on CN, so that the intermediate products can be transformed into the target products more smoothly. To further support this point, the charge difference distribution and ELF of reactant and intermediates (Fig. S4-S6) are also employed to demonstrate the electron transfer and the bonding state of adsorbed species on photocatalysts. Because of the electron localization caused by the intercalated Sr atom, the area far from the localized region possesses low electron density. As a result, the NO molecules are more prone to be adsorbed on this area and transfer electrons to the photocatalyst. Similarly, some intermediates tend to capture more localized electrons from the region with high electron density. Therefore, the covalent interaction between adsorbed species and CN-Sr become more stronger than that of the CN. The increased reactants and intermediates activation are contributed directly by the electron localization and the interlayered electronic channel in CN-Sr. Above all, the adsorption energy profile and adsorption state (Fig. 7) suggest that the enhanced activation of reactants and intermediates could promote the overall reaction efficiency selectivity in photocatalytic NO conversion.

#### 4. Conclusion

In order to promote the activity and selectivity of photocatalytic NO oxidation, the Sr-intercalated g- $\text{C}_3\text{N}_4$  has been designed and prepared. The normalized absorbance of  $\text{NO}_2^-$  and  $\text{NO}_3^-$  by in situ DRIFTS could help quantify the yield of the target products and investigate the selectivity of NO photocatalytic oxidation. Due to the intercalated Sr atom, the vertical charge channel has been established; the light absorption ability and charge separation efficiency have been accelerated. Most importantly, the electron localization has been constructed on CN-Sr, leading to uneven electron distributions on the surface of CN layer. As a result, the  $\text{O}_2$  molecule, NO pollutant and intermediate products could exchange electrons with catalyst and get activated to produce more radicals and target products. In combination with in situ DRIFTS and DFT simulation results, we found that once the NO and intermediates were contacted on the surface of CN-Sr, it could be adsorbed on the surface and deplete electrons to the low electron density region of CN-Sr. The electron exchange of reactants on the surface of photocatalyst makes these adsorbed species have higher activation efficiency, which makes these intermediates easier to be destroyed by the active radicals. Thus the NO can be selectively transformed into target productions rather than toxic byproducts. The present work specified the route of transportation and transformation of photogenerated carriers, unraveled the mechanism of photocatalytic NO oxidation on Sr-intercalated g- $\text{C}_3\text{N}_4$  and thus achieved the efficient and safe air purification.

#### Acknowledgements

This work was supported by the National Natural Science Foundation of China (51478070, 21777011 and 21501016), the National Key R&D Plan (2016YFC02047), the Innovative Research Team of Chongqing (CXTDG201602014), the Key Natural Science Foundation of Chongqing (cstc2017jcyjBX0052) and Innovation Research Project from CTBU (173014). The authors also acknowledge the AM-HPC in Suzhou, China for computational support.

Table 1

Adsorption energy and the total charge of species adsorb on CN and CN-Sr.  $E_{\text{ads}}$  stand for the adsorption energy for  $\text{O}_2$  molecules. Negative means heat release for  $E_{\text{ads}}$ .

sample	NO	cis- $\text{N}_2\text{O}_2$	trans- $\text{N}_2\text{O}_2$	$\text{NO}_2^-$	$\text{NO}_3^-$
	$E_{\text{ads}}$ , eV	$E_{\text{ads}}$ , eV	$E_{\text{ads}}$ , eV	$E_{\text{ads}}$ , eV	$E_{\text{ads}}$ , eV
CN	-0.16	-0.24	-0.29	-0.23	-0.80
CN-Sr	-0.73	-0.57	-0.79	-0.96	-1.92



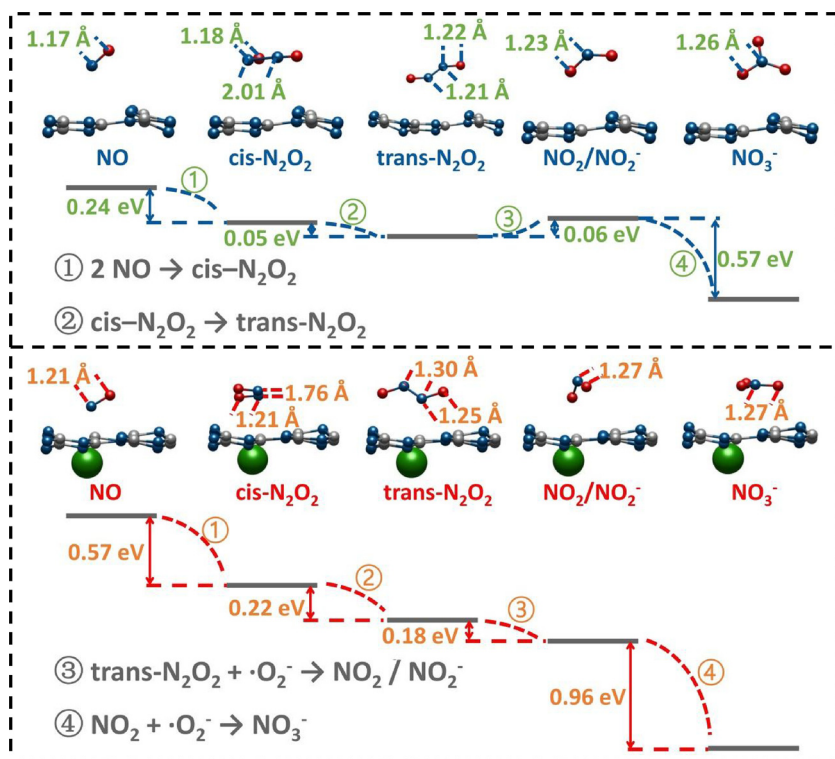


Fig. 7. DFT calculated adsorption energy and bond length of several major intermediate adsorption products (upward for CN and downward for Sr intercalated CN), all lengths are given in Å.

## Appendix A. Supplementary data

Supplementary material related to this article can be found, in the online version, at doi:<https://doi.org/10.1016/j.apcatb.2018.03.054>.

## References

- [1] P. Forzatti, I. Nova, E. Tronconi, *Angew. Chem. Int. Ed.* 121 (2009) 8516–8518.
- [2] Z. Ai, W. Ho, S. Lee, L. Zhang, *Environ. Sci. Technol.* 43 (2009) 4143–4150.
- [3] G. Dong, D. Jacobs, L. Zang, C. Wang, *Appl. Catal. B-Environ.* 218 (2017) 515–524.
- [4] S. Jin, G. Dong, J. Luo, F. Ma, C. Wang, *Appl. Catal. B-Environ.* 227 (2018) 24–34.
- [5] H. Wang, Y. Sun, G. Jiang, Y. Zhang, H. Huang, Z. Wu, S.C. Lee, F. Dong, *Environ. Sci. Technol.* 52 (2018) 1479–1487.
- [6] Y. Bai, L. Ye, L. Wang, X. Shi, P. Wang, W. Bai, P. Wong, *Appl. Catal. B-Environ.* 194 (2016) 98–104.
- [7] J. Ding, Z. Dai, F. Qin, H. Zhao, S. Zhao, R. Chen, *Appl. Catal. B-Environ.* 205 (2016) 281–291.
- [8] D. Scanlon, C. Dunnill, J. Buckeridge, S. Shevlin, A. Logsdail, S. Woodley, C. Catlow, M. Powell, R. Palgrave, I. Parkin, *Nat. Mater.* 12 (2013) 798–801.
- [9] X. Chen, L. Liu, P. Yu, S. Mao, *Science* 331 (2011) 746–750.
- [10] X. Li, W. Zhang, W. Cui, Y. Sun, G. Jiang, Y. Zhang, H. Huang, F. Dong, *Appl. Catal. B-Environ.* 221 (2018) 482–489.
- [11] J. Kou, R.S. Varma, *Nanoscale* 5 (2013) 8675–8679.
- [12] Z. Chen, J. Xu, Z. Ren, Y. He, G. Xiao, *Catal. Commun.* 41 (2013) 83–86.
- [13] Y. Sun, X. Xiao, X. Dong, F. Dong, W. Zhang, *Chin. J. Catal.* 38 (2017) 217–226.
- [14] C. Liu, K. Dubois, M. Louis, A. Vorushilov, G. Li, *ACS Catal.* 3 (2013) 655–662.
- [15] L. Liu, F. Gao, H. Zhao, Y. Li, *Appl. Catal. B-Environ.* 134–135 (2013) 349–358.
- [16] Y. Huang, Y. Liang, Y. Rao, D. Zhu, J. Cao, Z. Shen, W. Ho, S.C. Lee, *Environ. Sci. Technol.* 51 (2017) 2924–2933.
- [17] S. Ghosh-Mukerji, H. Haick, Y. Paz, J. Photoch., *Photo. A-Chem.* 160 (2003) 77–85.
- [18] S. Ghoshmukerji, H. Haick, M. Schwartzman, Y. Paz, *J. Am. Chem. Soc.* 123 (2001) 10776–10777.
- [19] Z. Ni, W. Zhang, G. Jiang, X. Wang, Z. Lu, Y. Sun, X. Li, Y. Zhang, F. Dong, *Chin. J. Catal.* 38 (2017) 1174–1183.
- [20] W.C. Wan, S. Yu, F. Dong, Q. Zhang, Y. Zhou, *J. Mater. Chem. A* 4 (2016) 7823–7829.
- [21] Q. Zhang, Y. Huang, S. Peng, Y. Zhang, Z. Shen, J.J. Cao, W. Ho, S.C. Lee, D.Y.H. Pui, *Appl. Catal. B-Environ.* 204 (2017) 346–357.
- [22] G. Dong, W. Ho, L. Zhang, *Appl. Catal. B-Environ.* 168–169 (2015) 490–496.
- [23] X. Lang, H. Ji, C. Chen, W. Ma, J. Zhao, *Angew. Chem. Int. Ed.* 50 (2011) 3934–3937.
- [24] F. Parrino, A. Ramakrishnan, H. Kisch, *Angew. Chem. Int. Ed.* 47 (2008) 7107–7109.
- [25] X. Dong, W. Zhang, Y. Sun, J. Li, W. Cen, Z. Cui, H. Huang, F. Dong, *J. Catal.* 357 (2018) 41–50.
- [26] X. Wang, K. Maeda, A. Thomas, K. Takanabe, G. Xin, J. Carlsson, K. Domen, M. Antonietti, *Nat. Mater.* 8 (2009) 76–82.
- [27] J. Liu, H. Wang, M. Antonietti, *Chem. Soc. Rev.* 45 (2016) 2308–2326.
- [28] C. Ye, J. Li, Z. Li, X. Li, X. Fan, L. Zhang, B. Chen, C. Tung, L. Wu, *ACS Catal.* 5 (2015) 6973–6979.
- [29] J. Tiwari, Y. Seo, T. Yoon, G. Wang, W. Cho, M. Yousuf, A. Harzandi, D. Kang, K. Kim, P. Suh, *ACS Nano* 11 (2017) 742–751.
- [30] L. Azofra, D. MacFarlane, C. Sun, *Phys. Chem. Chem. Phys.* 18 (2016) 18507–18514.
- [31] Y. Zheng, Y. Jiao, Y. Zhu, Q. Cai, A. Vasiliev, L. Li, Y. Han, Y. Chen, S. Qiao, *J. Am. Chem. Soc.* 139 (2017) 3336–3339.
- [32] H. Yu, L. Shang, T. Bian, R. Shi, G. Waterhouse, Y. Zhao, C. Zhou, L. Wu, C. Tung, T. Zhang, *Adv. Mater.* 28 (2016) 5080–5086.
- [33] Y. Li, S. Ouyang, H. Xu, X. Wang, Y. Bi, Y. Zhang, J. Ye, *J. Am. Chem. Soc.* 138 (2016) 13289–13297.
- [34] J. Li, W. Cui, Y. Sun, Y. Chu, W. Cen, F. Dong, *J. Mater. Chem. A* 5 (2017) 9358–9364.
- [35] T. Xiong, W. Cen, Y. Zhang, F. Dong, *ACS Catal.* 6 (2016) 2462–2472.
- [36] S. Grimme, *J. Comput. Chem.* 27 (2006) 1787–1799.
- [37] G. Kresse, J. Furthmüller, *Phys. Rev. B-Condens. Matter.* 54 (1996) 11169.
- [38] G. Kresse, J. Furthmüller, *Comput. Mater. Sci.* 6 (1996) 15–50.
- [39] J.P. Perdew, K. Burke, M. Ernzerhof, *Phys. Rev. Lett.* 77 (1996) 3865–3868.
- [40] B.P.E. Phys. Rev. B-Condens. Matter 50 (1994) 17953–17979.
- [41] G. Kresse, D. Joubert, *Phys. Rev. B-Condens. Matter.* 59 (1999) 1758–1775.
- [42] J. Heyd, *J. Chem. Phys.* 118 (2003) 8207–8215.
- [43] J. Heyd, *J. Chem. Phys.* 124 (2006) 219906.
- [44] W. Cui, J. Li, W. Cen, Y. Sun, S.C. Lee, F. Dong, *J. Catal.* 352 (2017) 351–360.
- [45] W. Cui, J. Li, F. Dong, Y. Sun, G. Jiang, W. Cen, S. Lee, Z. Wu, *Environ. Sci. Technol.* 51 (2017) 10682–10690.
- [46] S. Steinmann, T. Bahers, P. Sautet, *J. Mater. Chem. A* 5 (2017) 5115–5122.
- [47] Z. Lan, G. Zhang, X. Wang, *Appl. Catal. B-Environ.* 192 (2016) 116–125.
- [48] R. Bader, *Oxford University Press*, 1994.
- [49] B. Klingenberg, M. Vannice, *Appl. Catal. B-Environ.* 21 (1999) 19–33.
- [50] K. Hadjiivanov, H. Knozinger, *Phys. Chem. Chem. Phys.* 2 (2000) 2803–2806.
- [51] H. Miyata, S. Konishi, T. Ohno, F. Hatayama, *J. Chem. Soc. Faraday Trans. 91* (1995) 1557–1562.
- [52] J.L. Hardwick, J.C.D. Brand, *Can. J. Phys.* 54 (1976) 80–91.
- [53] K. Hadjiivanov, *Catal. Rev.* 42 (2000) 71–144.
- [54] H. Wang, W. He, X. Dong, H. Wang, F. Dong, *Sci. Bull.* 2018 (63) (2018) 117–125.
- [55] H. Wang, W. Zhang, X. Li, J. Li, W. Cen, Q. Li, F. Dong, *Appl. Catal. B-Environ.* 225 (2018) 218–227.